Simulation of fluid flow and time-lapse seismics. The CO_2 storage Sleipner-field case.

Gabriela B. Savioli[a,*], Juan E. Santos[b,c,d], José M. Carcione[e], Davide Gei[e]

[a] *Laboratorio de Ingeniería de Reservorios, Instituto del Gas y del Petróleo and Dto. de Ing. Química, Facultad de Ingeniería, Universidad de Buenos Aires Av. Las Heras 2214 Piso 3 C1127AAR Buenos Aires, Argentina gsavioli@fi.uba.ar*

[b] *CONICET, Instituto del Gas y del Petróleo, Facultad de Ingeniería, Universidad de Buenos Aires, Av. Las Heras 2214 Piso 3 C1127AAR Buenos Aires, Argentina*

[c] *Department of Mathematics, Purdue University, 150 N. University Street, West Lafayette, Indiana, 47907-2067, USA, santos@math.purdue.edu*

[d] *Universidad Nacional de La Plata, Argentina*

[e] *Istituto Nazionale di Oceanografia e di Geofisica Sperimentale (OGS), Borgo Grotta Gigante 42c, 34010 Sgonico, Trieste, Italy, jcarcione@inogs.it*

Abstract

We perform a time-lapse seismic characterization of the Sleipner aquifer due to CO_2 injection and storage. It is essential to built a suitable geological model based on a porous-media constitutive equation. This model considers a poroelastic description of the Utsira formation (a shaly sandstone), based on porosity and clay content, and takes into account the variation of the properties with pore pressure and fluid saturation. Moreover, the model considers the geometrical features of the formations, including the presence of shale seals and fractures. We also model fractal variations of the petrophysical properties. The numerical simulation of the CO_2-brine flow is based on the Black-Oil formulation, which uses the Pressure-Volume-Temperature (PVT) behavior as a simplified thermodynamic model. The corresponding equations are solved using a finite difference IMPES formulation.

Then, we compute synthetic seismograms on the basis of the resulting saturation and pore-pressure maps. Wave attenuation and velocity dispersion, caused by heterogeneities formed of gas patches, are described with White's mesoscopic

*Corresponding author, e-mail: gbsavioli@yahoo.com.ar, fax: +54-11-4514-3026

model to obtain an equivalent viscoelastic medium at the macroscale. The wave equation is solved in the space-frequency domain with a finite-element iterative domain decomposition algorithm.

The fluid simulator properly models the CO_2 injection, obtaining accumulations below the mudstone layers as injection proceeds. We are able to identify the time-lapse distribution of CO_2 from the synthetic seismograms, which show the typical pushdown effect.

The proposed methodology constitutes an important tool to monitor the CO_2 plume and analyze storage integrity, providing an early warning in the case any leakage may occur.

Keywords Multiphase fluid flow, CO_2 injection and storage, synthetic seismograms, finite differences, finite elements

1. Introduction

Capture and storage of carbon dioxide in deep saline aquifers and aging oil reservoirs is a valid alternative approach for reducing the amount of greenhouse gases in the atmosphere [1]. Saline aquifers are suitable as storage sites due to their large volume and their common occurrence in nature. The first industrial scale CO_2 injection project is the Sleipner gas field in the North Sea, where CO_2 separated from natural gas, is being injected in the Utsira formation, a highly permeable porous sandstone 800 m below the sea bottom. Within the formation, there are several mudstone layers which act as barriers to the vertical flow of the CO_2. Injection started in 1996 at a rate of about one million tonnes per year [1]-[2].

Nevertheless, very little is known about the behavior of stored CO_2 over very long periods. Numerical modeling of CO_2 injection and seismic monitoring are important tools to understand the long term behavior after injection and to test the effectiveness of CO_2 sequestration. Recent papers [3]-[5] successfully apply seismic modeling for monitoring the spatio-temporal distribution of CO_2 using assumed saturation maps. Instead, we introduce a methodology to model

the gas flow and monitor the storage. For this purpose, we perform numerical simulations of CO_2-brine flow and seismic wave propagation. We build a petrophysical model of the Utsira formation based on fractal porosity and clay content, taking into account the variation of properties with pore pressure and saturation [6]. This model also includes embedded mudstone layers of very low permeability that accumulate CO_2 but also allow its migration. The simultaneous flow of brine and CO_2 is modeled with the Black-Oil formulation for two-phase flow in porous media [7], which uses the PVT data as a simplified thermodynamic model [8]. The pressure map before the injection is assumed to be hydrostatic for which a reference porosity map is defined. The permeability is assumed to be anisotropic and is obtained from first principles as a function of porosity and grain sizes [6].

The wave propagation is based on an isotropic viscoelastic model that considers dispersion and attenuation effects. The complex P-wave and S-wave moduli are determined as follows: in the brine saturated mudstone layers we use a Zener model to represent the viscoelastic behavior of the material [9]; outside the mudstone layers, we use White's theory [10] to model P-wave attenuation, based on a model of porous layers alternately saturated with brine and CO_2. The results of the flow simulator, applied to the petrophysical (poro-viscoelastic) model, allows us to calculate the phase velocities and attenuation coefficients of the P and S waves in order to compute the synthetic seismograms.

The methodology is used to model CO_2 injection and flow and compute time-lapse seismograms corresponding to the Utsira aquifer at Sleipner field. It is possible to identify the spatio-temporal distribution of CO_2 after its injection over long periods of time. Attenuation and dispersion effects are clearly observed in the recorded traces. The synthetic seismograms show the progressive increase in CO_2 accumulations below the mudstone layers and the pushdown effect observed in field data [11]. Better results are obtained by updating the petrophysical properties (mainly porosity, permeability and dry-rock moduli). Since the effectiveness of the time-lapse seismic method depends on the survey plan and the properties of the storage site [12], these simulations may be used

to optimize the type of sources and the number and location of receivers to perform the seismic surveys.

2. THE BLACK-OIL FORMULATION OF TWO-PHASE FLOW IN POROUS MEDIA

The simultaneous flow of brine and CO_2 in porous media is described by the well-known Black-Oil formulation applied to two-phase, two component fluid flow [7]. We identify the CO_2 saturated aqueous phase (CO_2 and brine components, subindex b) with the oil phase and the CO_2 phase (subindex g) with the gas phase. In this way, the CO_2 component may dissolve in the aqueous phase but the brine component is not allowed to vaporize into the CO_2 phase. The differential equations are obtained by combining the mass conservation equations with Darcy's empirical Law.

The mass conservation equations are:

For the CO_2 component,

$$-\nabla \cdot (\rho_g \ v_g + C_{g,b} \ \rho_b \ v_b) + q_g = \frac{\partial \Big[\phi \left(\rho_g S_g + C_{g,b} \ \rho_b \ S_b\right)\Big]}{\partial t}; \quad (1)$$

for the brine component,

$$-\nabla \cdot (C_{b,b} \ \rho_b \ v_b) + q_b = \frac{\partial \Big[\phi (C_{b,b} \ \rho_b \ S_b)\Big]}{\partial t}, \qquad (2)$$

where ρ is density at reservoir conditions, v is Darcy velocity, S is saturation, q mass rate of injection per unit volume and ϕ is porosity. $C_{g,b}$, $C_{b,b}$ are the mass fractions of CO_2 and brine in the brine phase, respectively. In the Black-Oil formulation these fractions are computed using a simplified thermodynamic model as

$$C_{g,b} = \frac{R_s \ \rho_g^{SC}}{B_b \ \rho_b}, \quad C_{b,b} = \frac{\rho_b^{SC}}{B_b \rho_b}, \quad \rho_g = \frac{\rho_g^{SC}}{B_g} \qquad (3)$$

where R_s (CO_2 solubility in brine), B_g (CO_2 formation volume factor) and B_b (brine formation volume factor) are the PVT data. Also ρ_g^{SC} and ρ_b^{SC} are the CO_2 and brine densities at standard conditions. To estimate the Black-Oil PVT data we apply an algorithm developed by Hassanzadeh et al [8], which is summarized in subsection 5.2.

The empirical Darcy's Law gives the momentum balance for the fluids,

$$v_g = -\underline{\kappa}\frac{\kappa_{rg}}{\eta_g}(\nabla p_g - \rho_g g \nabla D), \tag{4}$$

$$v_b = -\underline{\kappa}\frac{\kappa_{rb}}{\eta_b}(\nabla p_b - \rho_b g \nabla D), \tag{5}$$

where D indicates depth, generally identified with the coordinate z, and g is the gravity constant. Also, p_g, p_b are the fluid pressures and $\underline{\kappa}$ is the absolute permeability tensor, assumed to be diagonal $\underline{\kappa} = \mathrm{diag}(\kappa_x, \kappa_y, \kappa_z)$. For $\beta = g, b$, the functions $k_{r\beta}$ and η_β are the relative permeability and viscosity of the β-phase, respectively.

Replacing equations (3)-(5) into equations (1)-(2) and dividing by ρ_g^{SC} and ρ_b^{SC}, the following nonlinear system of partial differential equations is obtained,

$$\nabla \cdot (\underline{\kappa}(\frac{\kappa_{rg}}{B_g \eta_g}(\nabla p_g - \rho_g g \nabla D) + \frac{R_s \kappa_{rb}}{B_b \eta_b}(\nabla p_b - \rho_b g \nabla D))) + \frac{q_g}{\rho_g^{SC}} = \frac{\partial\Big[\phi\left(\frac{S_g}{B_g} + \frac{R_s S_b}{B_b}\right)\Big]}{\partial t}, \tag{6}$$

$$\nabla \cdot (\underline{\kappa}\frac{\kappa_{rb}}{B_b \eta_b}(\nabla p_b - \rho_b g \nabla D)) + \frac{q_b}{\rho_b^{SC}} = \frac{\partial\Big[\phi\frac{S_b}{B_b}\Big]}{\partial t}. \tag{7}$$

Two algebraic equations relating the saturations and pressures, complete the system:

$$S_b + S_g = 1, \qquad p_g - p_b = P_C(S_b), \tag{8}$$

where P_C is the capillary pressure.

The unknowns for the Black-Oil model are the fluid pressures p_g, p_b and the saturations S_g, S_b for the CO_2 and brine phases, respectively. This flow model does not take into account chemical reactions.

The numerical solution is obtained with public-domain software BOAST [13] which solves the differential equations using the IMPES algorithm (IMplicit Pressure Explicit Saturation), based on a finite difference technique [7]. Finite differences is the standard in commercial reservoir simulators, and the improved versions use both structured and unstructured grids with local refinements to accurately represent reservoir geometry. The basic idea of IMPES is to obtain a single pressure equation by a combination of the flow equations. Once pressure is implicitly computed for the new time, saturation is updated explicitly. Next, we briefly describe IMPES for the system of equations (6), (7) and (8). The first step is to obtain the pressure equation, therefore equation (6) multiplied by B_g and equation (7) multiplied by $(B_b - R_s B_g)$ are added. In this way, the right-hand side of the combined equation is

$$B_g \frac{\partial\Big[\phi\left(\dfrac{S_g}{B_g} + \dfrac{R_s S_b}{B_b}\right)\Big]}{\partial t} + (B_b - R_s B_g)\frac{\partial\Big[\phi\dfrac{S_b}{B_b}\Big]}{\partial t}. \tag{9}$$

Using the chain rule to expand the time derivatives, and after some algebraic manipulations, the expression in (9) becomes:

$$\phi\Big[\frac{1}{\phi}\frac{d\phi}{dp_b} + S_g\left(-\frac{1}{B_g}\frac{dB_g}{dp_b}\right) + S_b\left(-\frac{1}{B_b}\frac{dB_b}{dp_b} + \frac{B_g}{B_b}\frac{dR_s}{dp_b}\right)\Big]\frac{\partial p_b}{\partial t}, \tag{10}$$

where all time derivatives of saturation have disappeared.

Defining the compressibilities as

Formation compressibility: $c_f = \dfrac{1}{\phi}\dfrac{d\phi}{dp_b}$,

Gas compressibility: $c_g = -\dfrac{1}{B_g}\dfrac{dB_g}{dp_b}$,

Brine compressibility: $c_b = -\frac{1}{B_b}\frac{dB_b}{dp_b} + \frac{B_g}{B_b}\frac{dR_s}{dp_b}$,

Total compressibility: $c_t = c_f + S_g c_g + S_b c_b$,

the following simply expression is obtained for (10),

$$\phi c_t \frac{\partial p_b}{\partial t}. \tag{11}$$

Finally, replacing p_g by $p_b + P_C(S_b)$ in the left side of the combined equation, the following pressure equation in p_b is obtained,

$$\begin{aligned} & B_g\Big[\nabla\cdot(\underline{\kappa}(\frac{\kappa_{rg}}{B_g\eta_g}(\nabla p_b - \rho_g g\nabla D) + \frac{R_s\kappa_{rb}}{B_b\eta_b}(\nabla p_b - \rho_b g\nabla D) + \frac{\kappa_{rg}}{B_g\eta_g}\nabla P_C))\Big] \\ & +(B_b - R_s B_g)\Big[\nabla\cdot(\underline{\kappa}\frac{\kappa_{rb}}{B_b\eta_b}(\nabla p_b - \rho_b g\nabla D))\Big] \\ & +B_g\frac{q_g}{\rho_g^{SC}} + (B_b - R_s B_g)\frac{q_b}{\rho_b^{SC}} = \phi c_t\frac{\partial p_b}{\partial t}. \end{aligned} \tag{12}$$

In the BOAST simulator, the system of nonlinear differential equations (7) and (12) is discretized using a block centered grid. The equations are linearized evaluating the pressure and saturation dependent functions (PVT parameters, viscosities, relative permeabilities and capillary pressure) using the pressure and saturation values at the previous time step. The pressure equation (12) is solved implicitly, applying a Block Successive Over Relaxation method (BSOR) to compute the solution of the linear system. The saturation equation (7) is solved explicitly, therefore stability restrictions are imposed to select the time step [14].

3. A VISCOELASTIC MODEL FOR WAVE PROPAGATION

One of the main phenomena occurring in rocks, in particular partially saturated with gas, is the mesoscopic-loss effect [10]-[9]. It is caused by heterogeneities in the fluid and solid phase properties greater than the pore size but much smaller than the predominant wavelengths. The mesoscopic-loss causes

wave attenuation and velocity dispersion. Because the mesoscopic-scale is typically on the order of centimeters, any finite-element or finite-difference numerical procedure based on Biot equations is impractical. To overcome this difficulty, we use an alternative approach, based on an equivalent viscoelastic medium.

Let ρ_s and ρ_f be the grain and fluid densities, respectively. The equation of motion in a 2D isotropic viscoelastic domain Ω with boundary $\partial\Omega$ can be stated in the space-frequency (x, ω) domain as

$$-\omega^2 \rho u - \nabla \cdot \sigma(u) = f(x, \omega), \quad \Omega \tag{13}$$

$$-\sigma(u)\nu = i\omega \mathcal{D} u, \quad \Gamma = \partial\Omega, \tag{14}$$

where $u = (u_x, u_z)$ is the displacement vector and

$$\rho = (1 - \phi)\rho_s + \phi\rho_f \tag{15}$$

is the bulk density.

Equation (14) is a first-order absorbing boundary condition [15], where

$$\mathcal{D} = \rho \begin{bmatrix} \nu_1 & \nu_2 \\ -\nu_2 & \nu_1 \end{bmatrix} \begin{bmatrix} v_P(\omega) & 0 \\ 0 & v_S(\omega) \end{bmatrix} \begin{bmatrix} \nu_1 & -\nu_2 \\ \nu_2 & \nu_1 \end{bmatrix},$$

with $\nu = (\nu_1, \nu_2)$ the unit outward normal on Γ and $v_P(\omega), v_S(\omega)$ the phase velocities of the compressional and shear waves at the frequency ω defined below in (17).

The stress tensor $\sigma(u)$ is defined in the space-frequency domain by

$$\sigma_{jk}(u) = \lambda_G(\omega)\nabla \cdot u\delta_{jk} + 2\mu(\omega)\varepsilon_{jk}(u), \quad \Omega, \tag{16}$$

where $\varepsilon_{jk}(u)$ denotes the strain tensor and δ_{jk} is the Kroenecker delta. The Lamé coefficients $\lambda_G(\omega)$ and $\mu(\omega)$ are complex and frequency dependent and are determined as follows. In the brine saturated mudstone layers these coefficients are obtained using a Zener model [9]. Outside the mudstone layers we consider P-wave attenuation due to wave induced fluid flow at mesoscopic scale using a model of porous layers alternately saturated with brine and CO_2, respectively [10]. This approach yields a complex and frequency dependent P-wave modulus

$E(\omega) = \lambda_G(\omega) + 2\mu(\omega)$ for the formation. S-wave attenuation is also taken into account by making the shear modulus $\mu(\omega)$ complex and frequency dependent using another relaxation mechanism related to the P-wave mechanism [5].

Both, Zener and White models, require the knowledge of the bulk modulus K_s and density ρ_s of the solid grains, the bulk and shear modulus K_m and μ_m as well as the porosity ϕ and permeabilities κ_x, κ_z of the solid matrix. They also need the fluid bulk modulus and viscosity. The determination of these parameters is explained in subsection 5.1.

The phase velocities $v(\omega)$ and quality factors $Q(\omega)$ are defined by the relations

$$v_t(\omega) = \left[\mathrm{Re}\left(\frac{1}{vc_t(\omega)}\right)\right]^{-1}, \qquad Q_t(\omega) = \frac{\mathrm{Re}(vc_t(\omega)^2)}{\mathrm{Im}(vc_t(\omega)^2)}, \quad t = P, S, \tag{17}$$

where $vc_t(\omega)$ are the complex and frequency dependent compressional velocities defined as

$$vc_P(\omega) = \sqrt{\frac{E(\omega)}{\rho}}, \quad vc_S(\omega) = \sqrt{\frac{\mu(\omega)}{\rho}}. \tag{18}$$

4. THE ITERATIVE DOMAIN DECOMPOSITION ALGORITHM

4.1. Weak Formulation

We proceed to formulate the variational form for viscoelastic waves:

Find $\widehat{u} \in [H^1(\Omega)]^2$ such that

$$-(\rho\omega^2\widehat{u}, \varphi) + \sum_{pq}(\sigma_{pq}(\widehat{u}), \varepsilon_{pq}(\varphi)) + i\omega \langle \mathcal{D}\widehat{u}, \varphi\rangle_\Gamma = (\widehat{f}, \varphi), \quad \varphi \in [H^1(\Omega)]^2.$$

Here $(f, g) = \int_\Omega f\overline{g}\, d\Omega$ and $\langle f, \overline{g}\rangle = \int_\Gamma f\overline{g}\, d\Gamma$ denote the complex $[L^2(\Omega)]^N$ and $[L^2(\Gamma)]^N$ inner products. Also, $H^1(\Omega)$ denotes the usual Sobolev space of functions in $L^2(\Omega)$ with first derivatives in $L^2(\Omega)$.

4.2. Finite Element Method

To define a global finite element method we employ the nonconforming finite element space based on rectangular elements first presented in [16] described below. For $h > 0$, let $\mathcal{T}_h$ be a quasiregular partition of $\overline{\Omega}$ such that $\overline{\Omega} = \cup_{j=1}^J \overline{\Omega}_j$

with Ω_j being rectangles of diameter bounded by h. Set $\Gamma_j = \partial\Omega \cap \partial\Omega_j$ and $\Gamma_{jk} = \Gamma_{kj} = \partial\Omega_j \cap \partial\Omega_k$, we denote by ξ_j and ξ_{jk} the centroids of Γ_j and Γ_{jk}, respectively.

We consider a nonconforming finite element space constructed using the following reference rectangular element:

$$\widehat{R} = [-1,1]^2 \qquad S_2(\widehat{R}) = \mathrm{Span}\left\{ \frac{1}{4} \pm \frac{1}{2}x - \frac{3}{8}\left((x^2 - \frac{5}{3}x^4) - (y^2 - \frac{5}{3}y^4) \right), \right.$$
$$\left. \frac{1}{4} \pm \frac{1}{2}y + \frac{3}{8}\left((x^2 - \frac{5}{3}x^4) - (y^2 - \frac{5}{3}y^4) \right) \right\}.$$

The four degrees of freedom associated with $S_2(\widehat{R})$ are the values at the mid points of the faces of $\widehat{R}$, i.e., the values at the nodal points $a_1 = (-1,0), a_2 = (0,-1), a_3 = (1,0)$ and $a_4 = (0,1)$. For example the basis function $\psi_1(x,y) = \frac{1}{4} - \frac{1}{2}x - \frac{3}{8}\left((x^2 - \frac{5}{3}x^4) - (y^2 - \frac{5}{3}y^4)\right)$ is such that $\psi_1(a_1) = 1$ and $\psi_1(a_j) = 0, j = 2,3,4$.

A useful property of employing nonconforming elements for wave propagation phenomena is that it almost halves the number of points per wavelength necessary to reach a given accuracy as compared with the standard bilinear elements [17].

Set $NC_j^h = S_2(\Omega_j)$ and define a nonconforming finite element space in the following manner

$$NC^h = \left\{ v \mid v_j : = v \mid_{\Omega_j} \in NC_j^h, j = 1, \ldots, J; \quad v_j(\xi_{jk}) = v_k(\xi_{jk}),\ \forall \{j,k\} \right\}.$$

The global nonconforming Galerkin procedure is defined as follows: find $\widehat{u}^h \in [NC^h]^2$ such that

$$-(\rho\omega^2 \widehat{u}^h, \varphi) + \sum_{pq} (\tau_{pq}(\widehat{u}^h), \varepsilon_{pq}(\varphi)) + i\omega \left\langle \left\langle \mathcal{D}\widehat{u}^h, \varphi \right\rangle \right\rangle_\Gamma = (\widehat{f}, \varphi), \quad \varphi \in [NC^h]^2,$$

where $\langle\langle \cdot, \cdot \rangle\rangle$ denotes the approximation of $\langle \cdot, \cdot \rangle$ on the boundary faces by the midpoint quadrature rule.

Instead of solving the global problem, we will use the parallelizable domain decomposition iterative hybridized procedure defined in [15]. This approach becomes a necessity when dealing with large 2D (or 3D) problems.

One of the main advantages of using nonconforming elements to solve wave propagation phenomena in parallel architectures is that the amount of information exchanged among processors in a domain decomposition iterative procedure is considerable reduced as compared to the case when conforming elements are employed. Besides, it is possible to obtain an estimate on the speed of convergence of the iterative domain decomposition procedure as a function of the mesh size h.

To define the iterative procedure, we introduce a set $\widetilde{\Lambda}^h$ of Lagrange multipliers λ_{jk}^h associated with the stress values $-\tau(\widehat{u}_j)\nu_{jk}(\xi_{jk})$:

$$\widetilde{\Lambda}^h = \{\lambda^h \colon \lambda^h|_{\Gamma_{jk}} = \lambda_{jk}^h \in [P_0(\Gamma_{jk})]^2 = [\Lambda_{jk}^h]^2\}.$$

Here $P_0(\Gamma_{jk})$ are constant functions on Γ_{jk}. Note that Λ_{jk}^h and Λ_{kj}^h are considered to be distinct.

Then, given an initial guess $\left(\widehat{u}_j^{h,0}, \lambda_{jk}^{h,0}, \lambda_{kj}^{h,0}\right) \in [NC_j^h]^2 \times [\Lambda_{jk}^h]^2 \times [\Lambda_{kj}^h]^2$, compute $\left(\widehat{u}_j^{h,n}, \lambda_{jk}^{h,n}\right) \in [NC_j^h]^2 \times [\Lambda_{jk}^h]^2$ as the solution of the equations

$$-(\rho\omega^2\widehat{u}_j^{h,n}, \varphi)_j + \sum_{pq}(\tau_{pq}(\widehat{u}^{h,n}), \varepsilon_{pq}(\varphi))_j + i\omega \left\langle\left\langle \mathcal{D}\widehat{u}_j^{h,n}, \varphi \right\rangle\right\rangle_{\Gamma_j}$$
$$+ \sum_k \left\langle\left\langle \lambda_{jk}^{h,n}, \varphi \right\rangle\right\rangle_{\Gamma_{jk}} = (\widehat{f}, \varphi)_j, \quad \varphi \in [NC_j^h]^2, \tag{19}$$

$$\lambda_{jk}^{h,n} = -\lambda_{kj}^{h,n-1} + i\beta_{jk}[\widehat{u}_j^{h,n}(\xi_{jk}) - \widehat{u}_k^{h,n-1}(\xi_{jk})], \qquad \text{on } \Gamma_{jk}. \tag{20}$$

It can be shown that

$$[\widehat{u}^{h,n} - \widehat{u}^h]^2 \to 0 \text{ in } [L^2(\Omega)]^2 \quad \text{when} \quad n \to \infty,$$

so that in the limit the global nonconforming Galerkin approximation is obtained [15].

5. PETROPHYSICAL, FLUID-FLOW AND SEISMIC DATA

In this section, we describe the procedure used to determine the petrophysical and fluid-flow parameters needed in the Black-Oil and seismic simulations.

5.1. A petrophysical model for the Utsira formation

The pressure dependence of properties is based on the following relationship between porosity and pore pressure $p(t) = S_b p_b(t) + S_g p_g(t)$,

$$\frac{(1-\phi_c)}{K_s}(p(t) - p_H) = \phi_0 - \phi(t) + \phi_c \ln \frac{\phi(t)}{\phi_0}, \tag{21}$$

where ϕ_c is a critical porosity, ϕ_0 is the initial porosity at hydrostatic pore pressure p_H and K_s is the bulk modulus of the solid grains [6]. The rock is formed with quartz (bulk modulus of 40 GPa) and clay (bulk modulus of 15 GPa). K_s is computed as the arithmetic average of the Hashin Shtrikman upper and lower bounds.

The relationship among horizontal permeability, porosity and clay content C is [6] ,

$$\frac{1}{\kappa_x(t)} = \frac{45(1-\phi(t))^2}{\phi(t)^3}\left(\frac{(1-C)^2}{R_q^2} + \frac{C^2}{R_c^2}\right), \tag{22}$$

where R_q and R_c are the average radii of the sand and clay grains.

Also, as permeability is anisotropic, we assume the following relationship between horizontal and vertical permeability κ_z [6]

$$\frac{\kappa_x(t)}{\kappa_z(t)} = \frac{1-(1-0.3a)\sin \pi S_b}{a(1-0.5\sin \pi S_b)}, \tag{23}$$

where a is the permeability-anisotropy parameter.

The bulk modulus of the dry matrix, K_m, is computed using the Krief equation [18] as follows:

$$K_m(t) = K_s(1-\phi(t))^{A/(1-\phi(t))}. \tag{24}$$

Assuming a relation $K_m/\mu_m = K_s/\mu_s$, we set

$$\mu_m(t) = \mu_s(1-\phi(t))^{A/(1-\phi(t))}. \tag{25}$$

Using the moduli K_s, K_m, μ_m, the porosity ϕ and permeabilities κ_x, κ_z, as well as the fluids bulk moduli and viscosities (computed using the Peng-Robinson model [19]), we determine the complex and frequency dependent Lamé coefficients $\lambda(\omega), \mu(\omega)$ as explained in Section 3.

Relative permeabilities and capillary pressure as functions of CO_2 saturation are represented by the following potential models [14]:

$$\kappa_{rg}(S_g) = \kappa^*_{rg}\big(\frac{S_g - S_{gc}}{1 - S_{gc} - S_{bc}}\big)^{n_g}, \tag{26}$$

$$\kappa_{ro}(S_g) = \kappa^*_{ro}\big(\frac{1 - S_g - S_{bc}}{1 - S_{gc} - S_{bc}}\big)^{n_o}, \tag{27}$$

$$P_C(S_g) = P^*_C\big(\frac{S_g - S_{gc}}{1 - S_{gc} - S_{bc}}\big)^{n_c}, \tag{28}$$

where κ^*_{rg}, κ^*_{ro}, P^*_C are the maximum values of the curves and the exponents n_g, n_o, n_c determine the curvature. S_{gc}, S_{bc} are the saturations at which CO_2 and brine phases become mobile, respectively.

5.2. The Black Oil fluid model

The PVT data, R_s and B_b, can be expressed in terms of the equilibrium properties obtained from an equation of state as presented in [8] and [20], i.e.,

$$R_s = \frac{\widetilde{\rho}^{SC}_b \chi_g}{\widetilde{\rho}^{SC}_g (1 - \chi_g)}, \qquad B_b = \frac{\rho^{SC}_b}{\rho_b (1 - \omega_g)}, \tag{29}$$

where $\widetilde{\rho}^{SC}_b$ and $\widetilde{\rho}^{SC}_g$ are the brine and CO_2 molar densities at standard conditions, respectively, χ_g and ω_g are the CO_2 mole and mass fractions in the brine phase. The molar density is related to the mass density through the molecular weight. While the CO_2 molecular weight (M_g) and mass density at standard conditions are known, these properties for the brine phase must be estimated. The brine molecular weight (M_b) is simply computed from the mole fractions χ_{salt} of NaCl and χ_{H_2O} of H_2O. The brine mass density at standard conditions, ρ^{SC}_b, is estimated following the Rowe and Chou correlation as given in formulas (B6)-(B14) of [8]. Once ρ^{SC}_b is computed, ρ_b at reservoir conditions is obtained using the approach of García, as stated in [8],

$$\rho_b = \frac{1 + (M_g/M_b)(\chi_g/(1 - \chi_g))}{(V_m/M_b)(\chi_g/(1 - \chi_g)) + 1/\rho_b}, \tag{30}$$

where V_m is a partial molar volume, computed as a function of temperature T (°C) as in formula (21) of [8]:

$$V_m = 37.51 - 9.585x10^{-2}T + 8.74x10^{-4}T^2 - 5.044x10^{-7}T^3. \quad (31)$$

To determine χ_g, we apply the following relationship

$$\chi_g = \frac{m_g}{m_g + 55.508 + \nu m_s}, \quad (32)$$

where m_g is the molality of CO_2 in saline water, m_s is the salt molality and ν is the stoichiometric number of ions in the dissolved salt. In order to compute m_g we use

$$m_g = \frac{m_g^o}{\gamma_g^*}, \quad (33)$$

where m_g^o is the molality of CO_2 in pure water and γ_g^* the activity coefficient.

To obtain m_g^o for each pressure and temperature, we solve iteratively the thermodynamic nonlinear equations (B1)-(B5) in [8]. These equations involve H_2O and CO_2 molar volumes, fugacities and activity coefficients. The CO_2 molar volume is computed using the Peng-Robinson model [19]. Also, γ_g^* is obtained using the Rumpf model, as stated in equation (A6) in Spycher & Pruess [20].

Once χ_g is computed, the CO_2 mass fraction in the aqueous phase ω_g is obtained from the relation:

$$\omega_g = \chi_g \frac{M_g}{M_{aq}}. \quad (34)$$

Here M_{aq} is the aqueous molecular weight, given by

$$M_{aq} = \chi_g M_g + \chi_{H_2O} M_{H_2O} + \chi_{salt} M_{salt}. \quad (35)$$

Finally, the viscosity, density and bulk modulus of CO_2 are obtained from the Peng-Robinson equations as a function of temperature and pore pressure.

6. NUMERICAL EXPERIMENTS

To test the proposed methodology, we consider a model of the Utsira formation having 1.2 km in the x-direction, 10 km in the y-direction and 0.4 km

in the z-direction (top at 0.77 km and bottom at 1.17 km b.s.l.). The pressure-temperature conditions are $T = 31.7z + 3.4$, where T is the temperature (in ^{o}C) and z is the depth (in km b.s.l.); $p_H = \rho_b g z$ is the hydrostatic pressure, with $\rho_b = 1040$ kg/m^3 the density of brine and g the gravity constant. Within the formation, there are several mudstone layers which act as barriers to the vertical motion of the CO_2.

The initial porosity ϕ_0 (at hydrostatic pore pressure) for the Utsira sandstone is assumed to have a fractal spatial distribution, obtained as follows. First, we generate a fractal porosity distribution, based on the so-called von Karman self-similar correlation functions. These models are widely used in the statistical characterization of heterogeneities for different applications. The fractal porosity is obtained with the following relation

$$\phi_0(x, z) = \langle \phi_0 \rangle + f(x, z). \tag{36}$$

In (36) $\langle \phi_0 \rangle$ denotes the spatial average of $\phi_0(x, z)$ and $f(x, z)$ is a fractal field representing the spatial fluctuation of $\phi_0(x, z)$, for which the spectral density is given by [21]

$$S_d(r_x, r_z) = N_0(1 + R^2\alpha^2)^{-(H+E/2)}. \tag{37}$$

Here $R = \sqrt{r_x^2 + r_z^2}$ is the radial wavenumber, α the correlation length, H is a self-similarity coefficient ($0 < H < 1$), N_0 is a normalization constant and E is the euclidean dimension. The von Karman correlation (37) describes a self-affine, fractal processes of fractal dimension $D = E + 1 - H$ at a scale smaller than α. For this application we take $E = 2$ and $D = 2.2$ and $\langle \phi_0 \rangle = 36.7$ %. The correlation length value was taken to be 2 % of the domain size. We generated a porosity field, by choosing the variance parameter in the fractal generator. Horizontal and vertical permeabilities were determined by using equations (22) and (23), considering an anisotropy parameter $a = 0.1$ and a fixed clay content $C = 6$ %. The minimum, average and maximum porosities obtained are 32.5 %, 36.7 % and 38.3 %. The associated vertical permeabilities are 0.1, 0.12 and 0.145 D. The mudstone layers are not completely sealed, having constant porosity and vertical permeability values of 24 % and 0.033 D. Besides they have openings,

that will give a path for the upward migration of CO_2. The top and bottom of the Utsira formation have constant porosity and vertical permeability values of 22 % and 0.02 D. The initial porosity and vertical permeability fields can be observed in Figures 1 and 2 a), respectively.

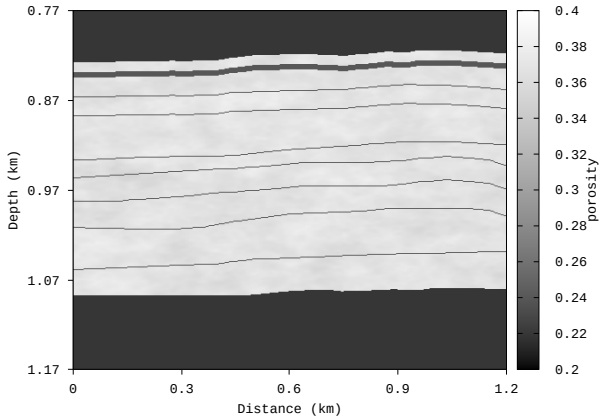

Figure 1: Initial porosity distribution before CO_2 injection.

6.1. CO_2 injection

CO_2 is injected during seven years in the Utsira formation at a constant flow rate of one million tons per year. The injection point is located at the bottom of the formation: $x = 0.6$ km, z =1.082 km. The simulation uses a mesh with equally-spaced blocks in each direction: $n_x = 300$ in the x-direction, $n_y = 5$ in the y-direction and $n_z = 400$ in the z-direction. Actually the model is 2.5D since the properties are uniform along the y-direction, which has an extension of 10 km. The source is located at the third grid point along this direction. To satisfy the CFL stability condition due to IMPES formulation [14], the time step is 0.125 d. With this choice of the mesh and time step, we check that the results of the BOAST simulator satisfy the mass conservation condition. Recall that the petrophysical properties of the formation are time dependent due to the CO_2 injection and consequent increase in pore fluid pressure (c.f. (21), (22), (23)) but they change at a much slower rate than pressure and saturations. As

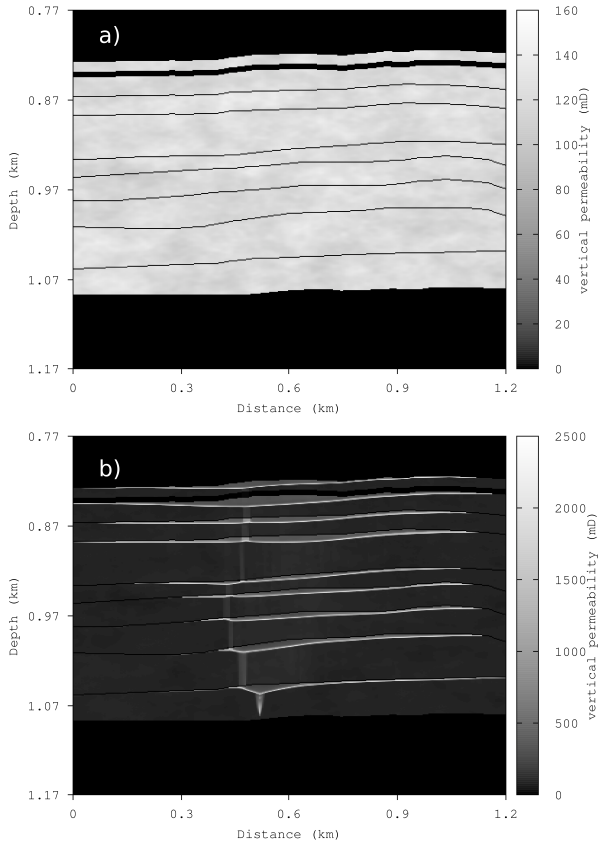

Figure 2: Vertical permeability distribution: a) before CO_2 injection and b) after 7 years of CO_2 injection.

a consequence, we have two time scales, and we use a much larger time step to update petrophysical properties than to run the flow simulator. In this work, the petrophysical properties are updated every year.

Figures 3 a), b) and c) show 2D vertical slices (corresponding to $n_y = 3$) of the CO_2 saturation fields after one, three and seven years of CO_2 injection, respectively. In all the cases, CO_2 accumulations below the mudstone layers can be observed. As injection proceeds, part of the injected fluid migrates upwards due to the openings in the mudstone layers that generate chimneys, and the vertical fluid flow is ruled by the vertical permeability. As CO_2 saturation

increases, vertical permeability updated with equation (23) also increases, in particular in the mudstone layers. This allows an increase in the CO_2 upward motion across the layers with the resulting low CO_2 saturations levels observed between layers. As a consequence, CO_2 chimneys become less defined as injection time increases, as it can be seen in Figures 3 a), b) and c). A 2D slice (at $n_y = 3$) of the saturation dependent vertical permeability distribution after seven years of CO_2 injection is shown in Figure 2 b). Porosity and horizontal permeability depending only on pressure suffer little changes and are not shown for brevity. Figure 4 displays the difference between CO_2 and brine pressure (capillary pressure) after seven years of injection. As CO_2 saturation increases, flow is more affected by capillary forces.

6.2. Seismic Monitoring

In this section, we analyze the capability of seismic monitoring to identify zones of CO_2 accumulation and migration. With this purpose, we use 2D slices of CO_2 saturation and fluid pressure obtained from the flow simulator to construct a 2D model of the Utsira formation. The iterative procedure given in equations (19)-(20) is used to compute the time Fourier transforms of the displacement vector for 200 equally spaced temporal frequencies in the interval $(0, 200\text{Hz})$. The seismic source is a spatially localized plane wave of main frequency 60 Hz located at $z = 772$ m. A line of receivers is located at the same depth to record the Fourier transforms of the vertical displacements. Then, a discrete inverse Fourier transform is employed to obtain the data used for the synthetic seismograms.

Initially, we show the pre-injection results at full brine saturation. Figures 5 a) and 6 a) display the spatial distribution of the P-wave phase velocity v_P and S-wave phase velocity v_S, respectively. Besides, Figure 7 a) shows the synthetic seismogram before the injection, where the mudstone layers in Figures 5 a) and 6 a) are clearly identified.

Figures 7 b), c) and d) display seismograms after one, three and seven years of CO_2 injection associated with the CO_2 saturations shown in Figures 3 a),

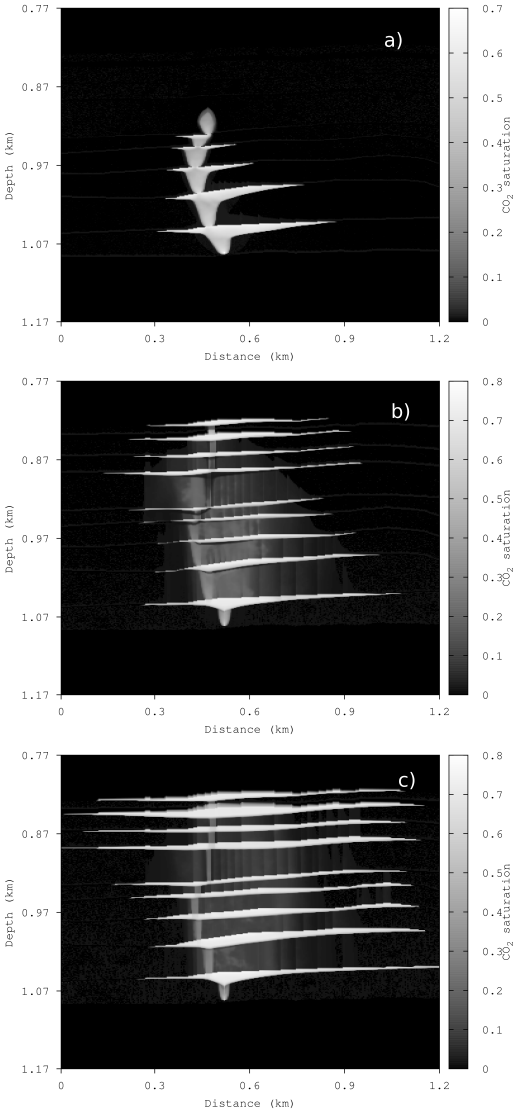

Figure 3: CO_2 saturation distribution: a) after one year of CO_2 injection, b) after three years of CO_2 injection and c) after seven years of CO_2 injection.

b) and c), respectively. A standard f-k filter is applied to the seismic sections. The reflections seen in those seismograms show the progressive increase in CO_2 accumulations below the mudstone layers as the injection proceeds. In partic-

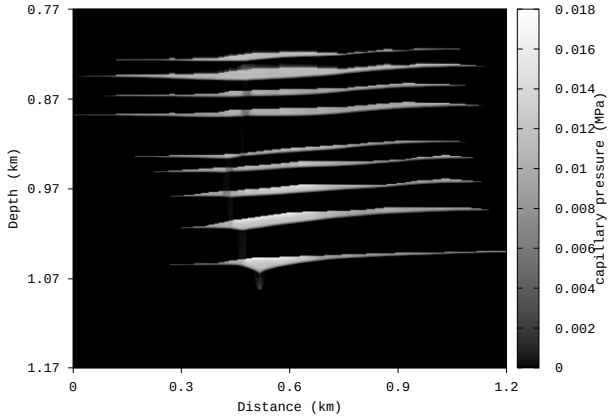

Figure 4: Capillary pressure distribution after seven years of CO_2 injection.

ular, the pushdown effect observed in the real seismograms [11] due to CO_2 accumulations is clearly observed (Figure 7 d)). Figures 5 b) and 6 b) display P and S-wave phase velocities v_P and v_S after seven years of CO_2 injection, predicted by White's model. It can be observed the reduction in the P-wave velocities in zones of CO_2 accumulation.

7. CONCLUSIONS

We have performed numerical simulations of CO_2-brine flow and seismic wave propagation to model and monitor CO_2 storage in a saline aquifer. The flow simulator considers the CO_2 solubility in brine through a simplified thermodynamic model, with CO_2 properties determined by the Peng-Robinson equations. We have built a petrophysical model of a shaly sandstone based on fractal porosity and considering the variation of its properties with pore pressure and fluid saturation. The wave propagation simulator takes into account wave velocity changes due to the presence of heterogeneous CO_2 accumulations and attenuation effects due to the presence of mesoscopic scale heterogeneities caused by patches of carbon dioxide. The proposed methodology has been applied to the Utsira formation, which contains several thin low-permeability mudstone

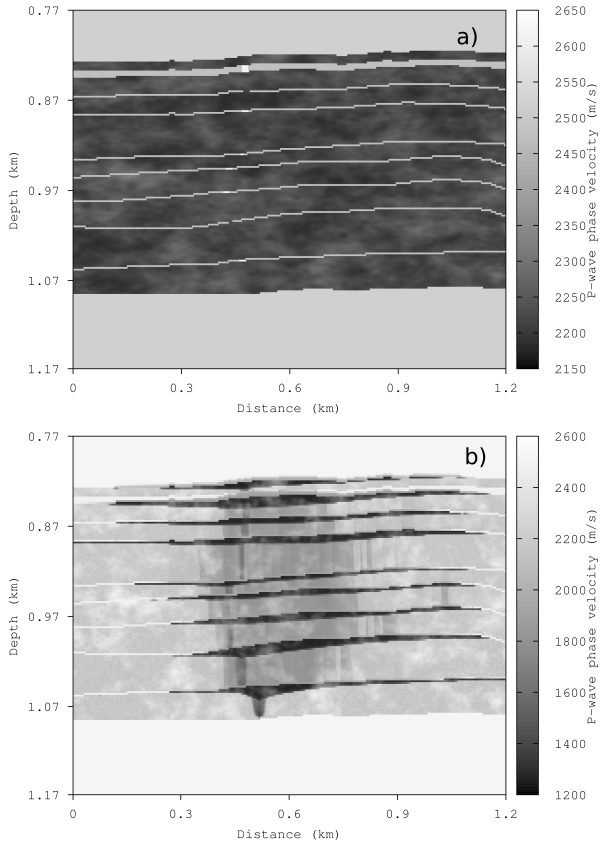

Figure 5: P-wave velocity: a) before CO_2 injection and b) after 7 years of CO_2 injection.

layers. These layers are not completely sealed and also have openings, allowing the upward migration of CO_2 .

The fluid-flow simulator yields CO_2 accumulations below the mudstone layers. Taking into account the time-lapse variations of the petrophysical properties (with vertical permeability being the more affected property by this updating), the corresponding synthetic seismograms resemble the real seismic data. In particular, regions of low saturations between layers and less defined chimneys are obtained. The reflections seen in the seismograms show the progressive increase in CO_2 accumulations below the mudstone layers, in particular, the pushdown effect is clearly observed.

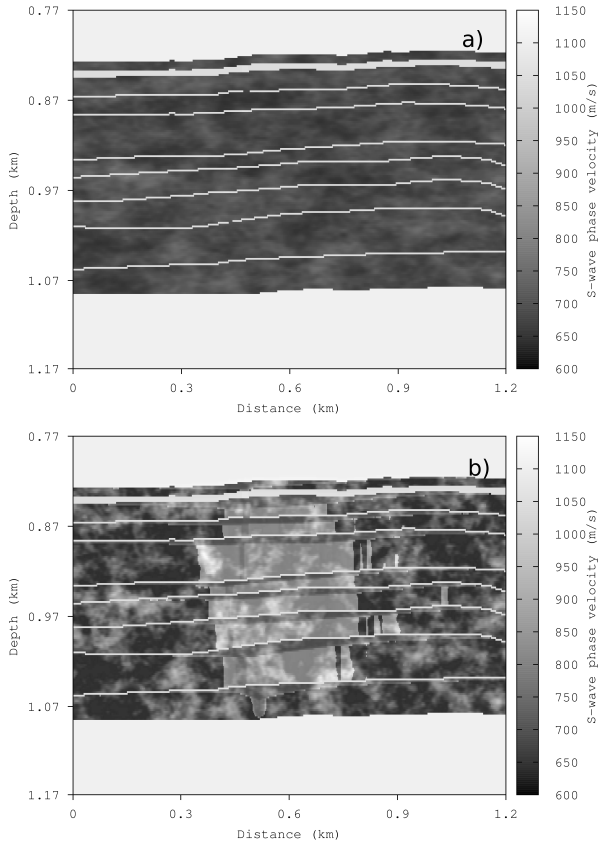

Figure 6: S-wave velocity: a) before CO_2 injection and b) after 7 years of CO_2 injection.

Summarizing, this methodology constitutes an important tool to monitor the migration and dispersal of the CO_2 plume, to analyze storage integrity and to make long term predictions.

8. ACKNOWLEDGEMENTS

This work was partially funded by CONICET, Argentina (PIP 0952) and Universidad de Buenos Aires (UBACYT 20020120100270). JMC and DG were partially supported by the CO2Monitor project.

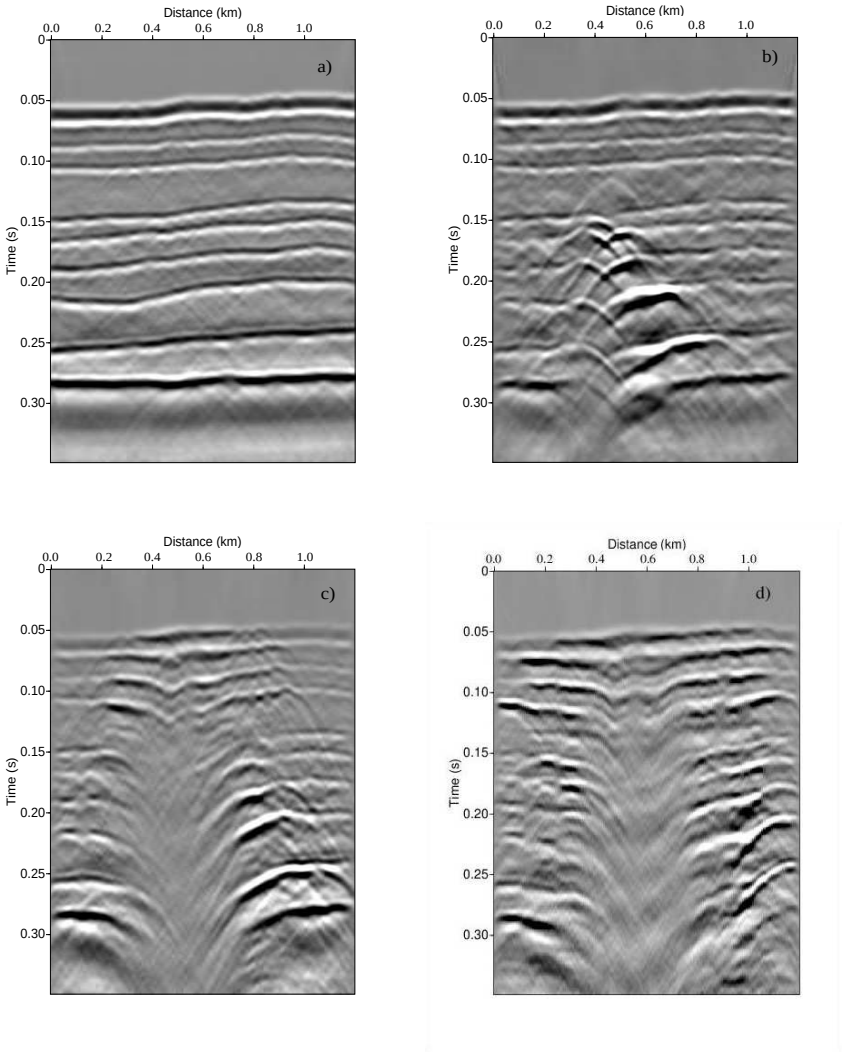

Figure 7: Synthetic seismograms: a) before CO_2 injection, b) after one year of CO_2 injection, c) after three years of CO_2 injection and d) after seven years of CO_2 injection

References

[1] R. Arts, A. Chadwick, O. Eiken, S. Thibeau, S. Nooner, Ten years of experience of monitoring CO_2 injection in the Utsira sand at Sleipner, offshore Norway, First break 26 (2008) 65–72.

[2] A. Chadwick, R. Arts, O. Eiken, 4D seismic quantification of a growing CO_2 plume at Sleipner, North Sea, Dore A G and Vincent B (Eds) Petroleum Geology: North West Europe and Global Perspectives - Proc. 6th Petroleum Geology Conference (2005) 1385–1399.

[3] J. M. Carcione, S. Picotti, P-wave seismic attenuation by slow-wave diffusion: Effects of inhomogeneous rock properties, Geophysics 71 (3) (2006) O1–O8.

[4] J. E. Santos, J. G. Rubino, C. L. Ravazzoli, Modeling mesoscopic attenuation in a highly heterogeneous Biot's medium employing an equivalent viscoelastic model, Proc. 78th Annual International Meeting SEG (Las Vegas) (2008) 2212–2215.

[5] S. Picotti, J. M. Carcione, D. Gei, G. Rossi, J. E. Santos, Seismic modeling to monitor CO_2 geological storage - 1 the Atzbach-Schwanenstadt gas field, Journal of Geophysical Research, 117 (2012) 1–18.

[6] J. M. Carcione, K. Helbig, H. B. Helle, Effects of pressure and saturating fluid on wave velocity and attenuation of anisotropic rocks, Int. J. Rock Mech. Min. Sci. 40 (2003) 389–403.

[7] K. Aziz, A. Settari, Petroleum Reservoir Simulation, Elsevier Applied Science Publishers, Great Britain, 1985.

[8] H. Hassanzadeh, M. Pooladi-Darvish, A. Elsharkawy, D. Keith, Y. Leonenko, Predicting PVT data for CO_2-brine mixtures for black-oil simulation of CO_2 geological storage, International Journal of Greenhouse Gas Control 2 (2008) 65–77.

[9] J. M. Carcione, Wave Fields in Real Media: Wave Propagation in Anisotropic, Anelastic, Porous and Electromagnetic Media, Vol. 38 of Handbook of Geophysical Exploration, Elsevier, 2nd edition, revised and extended, 2007.

[10] J. E. White, N. G. Mikhaylova, F. M. Lyakhovitskiy, Low-frequency seismic waves in fluid-saturated layered rocks, Izvestija Academy of Sciences USSR, Physics of Solid Earth 10 (1975) 654–659.

[11] R. A. Chadwick, D. Noy, R. Arts, O. Eiken, Latest time-lapse seismic data from Sleipner yield new insights into CO_2 plume development, Energy Procedia (2009) 2103–2110.

[12] R. A. Chadwick, G. Williams, N. Delepine, V. Clochard, K. Labat, S. Sturton, M. Buddensiek, M. Dillen, M. Nickel, A. Lima, R. Arts, F. Neele, G. Rossi, Quantitative analysis of time-lapse seismic monitoring data at the Sleipner CO_2 storage operation, The Leading Edge 29 (2010) 170–177.

[13] J. Fanchi, Principles of Applied Reservoir Simulation, Gulf Professional Publishing Company, Houston, Texas, 1997.

[14] G. Savioli, M. S. Bidner, Simulation of the oil and gas flow toward a well - a stability analysis, Journal of Petroleum Science and Engineering 48 (2005) 53–69.

[15] T. Ha, J. E. Santos, D. Sheen, Nonconforming finite element methods for the simulation of waves in viscoelastic solids, Comput. Meth. Appl. Mech. Engrg. 191 (2002) 5647–5670.

[16] J. Douglas, Jr., J. E. Santos, D. Sheen, X. Ye, Nonconforming Galerkin methods based on quadrilateral elements for second order elliptic problems, RAIRO Mathematical Modelling and Numerical Analysis (M2AN) 33 (1999) 747–770.

[17] F. I. Zyserman, P. M. Gauzellino, J. E. Santos, Dispersion analysis of a non-conforming finite element method for the Helmholtz and elastodynamic equations, Int. J. Numer. Meth. Engng. 58 (2003) 1381–1395.

[18] M. Krief, J. Garat, J. Stellingwerff, J. Ventre, A petrophysical interpretation using the velocities of P and S waves (full waveform sonic), The Log Analyst 31 (1990) 355–369.

[19] D. Y. Peng, K. I. Robinson, A new two-constant equation of state, Ind. Eng. Chem. Fundam. 15(1) (1976) 59–64.

[20] N. Spycher, K. Pruess, CO_2-H_2O mixtures in the geological sequestration of CO_2. II. partitioning in chloride brines at 12-100 C and up to 600 bar, Geochim. Cosmochim, Acta 69 13 (2005) 3309–3320.

[21] A. Frankel, R. W. Clayton, Finite difference simulation of seismic wave scattering: implications for the propagation of short period seismic waves in the crust and models of crustal heterogeneity, J. Geophys. Res. 91 (1986) 6465 – 6489.